PHYSICAL REVIEW B **110**, 064424 (2024)

Editors' Suggestion

Disentangling nucleation and propagation of magnetization reversal in exchange-biased thin films

M. Usama Hasan[1,2] and Geoffrey S. D. Beach[1,*]

[1]*Department of Materials Science and Engineering, Massachusetts Institute of Technology, Cambridge, Massachusetts 02139, USA*
[2]*Department of Materials and Metallurgical Engineering, Bangladesh University of Engineering and Technology, Dhaka 1000, Bangladesh*

(Received 3 April 2024; revised 31 July 2024; accepted 6 August 2024; published 22 August 2024)

The exchange-bias (EB) effect between a ferromagnet and antiferromagnet is crucial for many existing, as well as proposed, spintronic devices. For understanding, utilizing, and engineering EB, it is critical to understand how EB affects microscopic reversal processes, such as nucleation and propagation of domains, and how these in turn can govern macroscopic characteristics, including hysteresis loop shape. In this work, we disentangle the EB for nucleation and propagation by combining typical magneto-optical Kerr effect (MOKE) measurements with a method based on domain-wall (DW) motion. We show that MOKE is well suited for locating the nucleation sites and measuring the EB at these sites, while by measuring DW propagation, the effective field that the DW is subjected to can be quantified and the EB field inferred. Our experiments reveal that nucleation sites can experience wide-ranging EB fields, in contrast to propagation EB, and that there can be a significant difference in the EB that these two processes experience. Furthermore, we explore the consequences of unequal nucleation and propagation EB and discover that in addition to the EB of the nucleation site affecting measurements in the surrounding area, it can also give rise to asymmetry in hysteresis loop shape, something that has been observed widely but is not fully understood. This work describes surprising phenomena in systems that have been studied for decades, and we believe that the insights into how the interplay between different components of magnetization reversal can give rise to unexpected outcomes can be broadly useful for anyone working with coupled magnetic systems.

DOI: 10.1103/PhysRevB.110.064424

I. INTRODUCTION

The exchange-bias (EB) phenomenon pins a ferromagnet (FM) in a particular direction due to an exchange interaction at the interface with an antiferromagnet (AFM) [1–3]. This has found use in devices such as spin valves and magnetic read heads [4,5], and has been proposed as a component for emerging applications including field-free spin-orbit torque switching [6] and domain-wall based devices [7]. Since magnetization reversal is central to nearly all spintronic devices, understanding the ways in which EB can affect it is crucial for designing next-generation devices.

The principal microscopic processes underlying magnetization reversal in thin films, with or without EB, are domain nucleation and propagation [8–11], with sites of microscopic defects serving as heterogeneous nucleation centers. Macroscopic hysteresis loop (HL) properties are largely dictated by these two processes, and the presence of EB should affect both, although no studies have so far characterized it. The most well-known effect of EB is, of course, the shift of the HL along the field axis, which is explained by the symmetry-breaking effective field due to EB. However, EB can also make the HL shape asymmetric [3,12–15]. Various mechanisms validated to different extents have been proposed to explain this widely observed asymmetry, but many aspects remain poorly understood.

In this work, we disentangle the effect of EB on nucleation and propagation, and show that asymmetry in HL shape can arise quite generally in EB systems, even if the magnetization reversal pathway remains symmetric. Our experiments prove laser magneto-optical Kerr effect (MOKE) magnetometry to be a reliable way to determine EB at nucleation sites, revealing a surprisingly large site-to-site variation, while we find the propagation EB, evaluated using domain-wall (DW) creep, to be much more uniform and substantially different from many nucleation sites. We discover, both experimentally and with simulations, that EB determined from HL acquisition can be significantly influenced by a nucleation site that is far away, but also that differences in nucleation and propagation EB can give rise to asymmetric reversal characteristics. We quantify how these features depend on sample properties and experimental conditions, and finally show that in real samples even more complex interactions can take place due to multiple nucleation sites in proximity.

II. EXPERIMENTAL METHODS

The experiments were conducted in Ta(4)/Pt(3)/Co(0.8)/Pt(0.5)/$\mathrm{Co_{0.8}Ni_{0.2}O}(x)$ films, grown by dc magnetron sputtering (numbers in parentheses indicate thickness in nanometers) at room temperature on (100) thermally oxidized silicon substrates. All data were acquired using samples with x equal to 7 (S1), 8 (S2), and 10 (S3). The substrates were roughly rectangular in shape with side lengths ∼4−10 mm. For the metallic layers, Ar pressure of 3 mTorr

---

[*] Contact author: gbeach@mit.edu

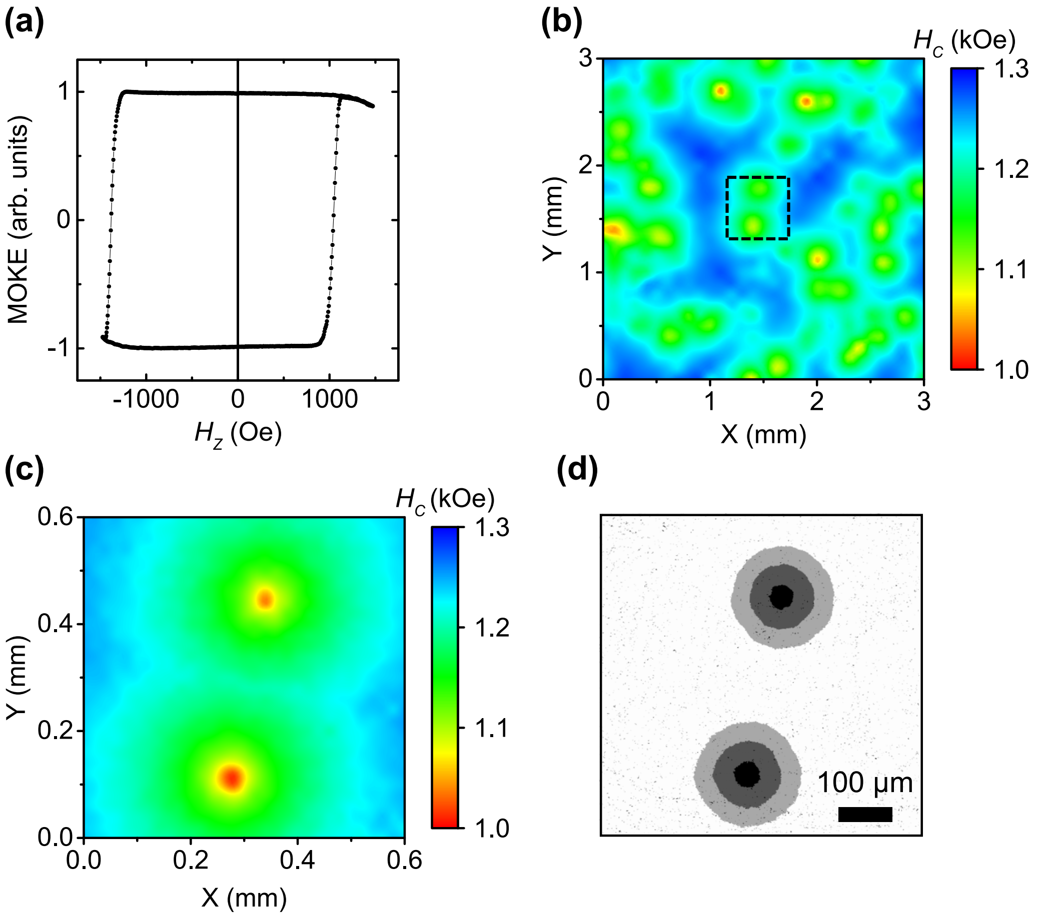

FIG. 1. (a) Typical large-area (9-mm^2) HL; $H_C = 1209$ Oe and $H_{\text{shift}} = -171$ Oe. (b) Coercivity map obtained from point-by-point (step size = 100 μm) HL acquisition from MOKE with a scanning stage. HL in (a) is the average of all HLs used to construct (b). (c) Higher-resolution (step size = 20 μm) coercivity map of region defined by black square in (b). (d) Reverse-domain growth of the same region using wide-field MOKE. Here, white (black, gray) denotes up (down) magnetization. The centers of the reversed domains correspond to the minima in (c). Down domains were nucleated using a −990-Oe, 200-ms pulse and then expanded using repeated −940-Oe, 350-ms pulses. The black, medium gray, and light gray regions indicate the extent of the reversed domains after 3, 10, and 17 pulses respectively. Data are from S1.

was used while $Co_{0.8}Ni_{0.2}O$ was grown by reactive sputtering under 1.6-mTorr Ar with P_{O_2} of 0.07 mTorr. Background pressure was $<5 \times 10^{-7}$ Torr and the materials were grown at an approximate rate of 2.8, 4.2, 1.1, and 2.4 nm/min respectively for Ta, Pt, Co, and $Co_{0.8}Ni_{0.2}O$. EB was set by a postdeposition field-cooling step from above 60° C (∼Néel temperature for our samples [16]) using a field >1.5 kOe, which exceeds the saturation field, oriented perpendicular to the substrate along the substrate-to-sample direction (defined as $+z$).

Space- and time-resolved magnetization reversal was studied using a wide-field MOKE microscope with an integrated scanning laser MOKE (∼10 μm laser spot) for local hysteresis loop acquisition. The laser (wavelength of 660 nm) was attenuated to sufficiently low power (∼1 mW) to ensure negligible temperature rise at the sample [17]. For sequential measurements, a full HL was acquired in 0.3 s, and a wait time of ∼ 3 s at positive remanence was incorporated between each instance of an HL acquisition. Incorporation of a wait period in the positive remanence state is important to revert the thermally activated AFM grain reversal that happens during the part of the HL when magnetization is oriented along $-z$. Thermally activated AFM grain reversal is a well-known phenomenon [18–20] that decreases EB, eventually causing sign reversal, when the FM is magnetized oppositely to the initial EB direction ($+z$).

III. RESULTS AND DISCUSSION

Figures 1(a) and 1(b) show, respectively, a spatially averaged out-of-plane hysteresis loop, analogous to those from typical macroscopic measurements such as vibrating sample magnetometry (VSM), along with a spatially resolved map of the local coercivity, H_C, within the same region in S1. The macroscopic loop is relatively square, with $H_C \approx 1200$ Oe and a loop shift $H_{\text{shift}} \approx -170$ Oe resulting from EB. The maximum field is limited by the experimental setup, but we have confirmed that it is sufficient to reach saturation (see the Appendix). The spatially resolved measurements, obtained by point-by-point HL acquisition [Fig. 1(b)], however, show substantial heterogeneity, suggesting that the macroscopic H_C and H_{shift} mask the underlying reversal processes. Figure 1(c) shows a higher-resolution H_C map (step size decreased to 20 from 100 μm) in the vicinity of two local H_C

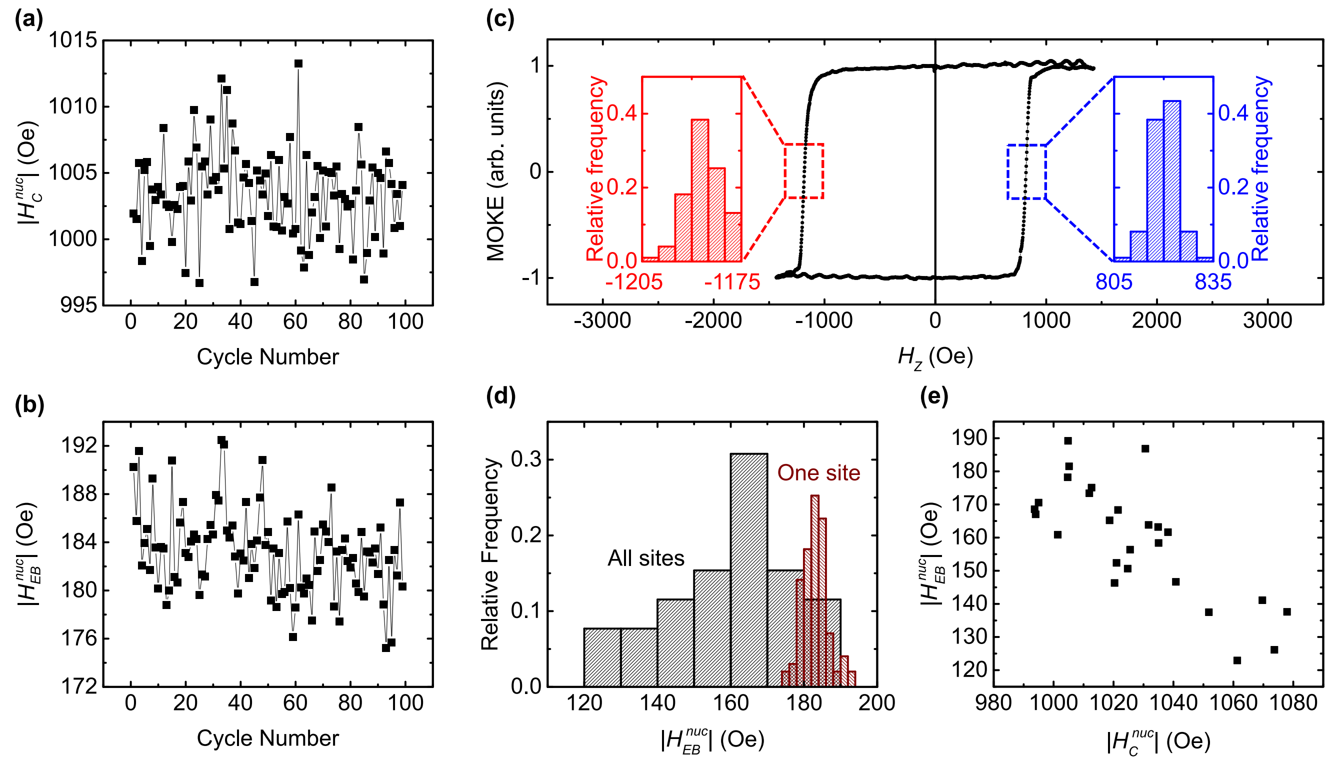

FIG. 2. (a) H_C^{nuc} and (b) $H_{\mathrm{EB}}^{\mathrm{nuc}}$ as a function of cycle number for the bottom nucleation site in Fig. 1(c). (c) HL obtained by averaging over all cycles. The insets show the stochasticity-driven distribution in the corresponding switching fields, which is the origin of the scatter seen in (a) and (b). (d) Comparison between the distribution of $H_{\mathrm{EB}}^{\mathrm{nuc}}$ for this site and for 26 nucleation sites measured throughout the entire sample. (e) Correlation between H_C^{nuc} and $H_{\mathrm{EB}}^{\mathrm{nuc}}$ for the ensemble of 26 nucleation sites.

minima, while Fig. 1(d) shows a nested set of wide-field MOKE images that reveal the origin of the spatially varying H_C. In the latter, after saturation parallel to H_{EB}, a 200-ms, 990-Oe reversed-field pulse was used to nucleate domains. A series of MOKE images was then obtained by applying field pulses to expand the reverse domains. Evidently, the H_C minima in Fig. 1(b) correspond to discrete nucleation sites, and the increase in H_C with increasing distance from the nucleation sites arises from the propagation delay of the nucleated domain walls as the reversal field is swept during loop acquisition. The macroscopic H_C is hence a complex function of the spatial distribution of nucleation sites, the distribution of nucleation fields at those sites, the field-dependent creep velocity, and the field-sweep rate. It is reasonable to anticipate a similarly complex relationship between the macroscopic loop shift (H_{shift}) and the underlying EB.

To disentangle this complexity, we characterized nucleation and propagation independently by examining reversal locally at an ensemble of nucleation sites, and in the region between nucleation sites, using domain-wall creep as a probe of local effective fields. Figures 2(a) and 2(b) show H_C^{nuc} and $H_{\mathrm{EB}}^{\mathrm{nuc}}$, respectively, from focused MOKE with the laser spot positioned over an exemplary nucleation site as a function of cycle number for repeated HL acquisition. The scatter of the data is random, and we do not see a significant systematic difference between the first cycle and the *n*th cycle, except a very small decrease in $H_{\mathrm{EB}}^{\mathrm{nuc}}$ as the cycling progresses, possibly due to thermally activated AFM grain reversal that did not fully revert (refer to Experimental Methods, Sec. II). Figure 2(c) shows the averaged HL of all cycles, together with distributions of the positive-sweep and negative-sweep switching fields observed during these ∼ 100 single-switching events. The cycle-to-cycle stochasticity in the nucleation field is what gives rise to the scatter in Figs. 2(a) and 2(b) leading to a relatively small variation in the shift field, as seen in Fig. 2(d). By contrast, the range of the mean shift field measured on 26 distinct nucleation sites spans > 60 Oe. This variation cannot be accounted for by stochasticity in the switching process and rather indicates that the exchange-bias field $H_{\mathrm{EB}}^{\mathrm{nuc}}$ in the vicinity of a nucleation site varies considerably from defect to defect. Although we cannot identify the nature of the defects nor the underlying origin of the variation in $H_{\mathrm{EB}}^{\mathrm{nuc}}$, we can rule out some possibilities by looking at the correlation between H_C^{nuc} and $H_{\mathrm{EB}}^{\mathrm{nuc}}$ for the ensemble of 26 nucleation sites. As shown in Fig. 2(e), there is weak negative correlation between the two, which may suggest a common contributor to variations in H_C^{nuc} and $H_{\mathrm{EB}}^{\mathrm{nuc}}$. Whatever parameter or combination of parameters is locally different at the nucleation sites causes H_C^{nuc} and $H_{\mathrm{EB}}^{\mathrm{nuc}}$ to vary in opposite senses. However, the relative variation from the mean for H_C^{nuc} is ∼ 5 times smaller than that of $H_{\mathrm{EB}}^{\mathrm{nuc}}$. Since EB is an interfacial effect and the perpendicular magnetic anisotropy of our samples is interfacial as well, we expect both H_C^{nuc} and $H_{\mathrm{EB}}^{\mathrm{nuc}}$ to vary as $\propto \frac{1}{t_{\mathrm{FM}} M_S}$, ruling out locally varying M_S and/or t_{FM} because that would cause a proportionate change of the same sense. We cannot rule out locally varying t_{AFM}, interfacial exchange J_{ex}, or AFM anisotropy K_{AFM}, and further experiments would be needed to come to a more informed conclusion. Nevertheless,

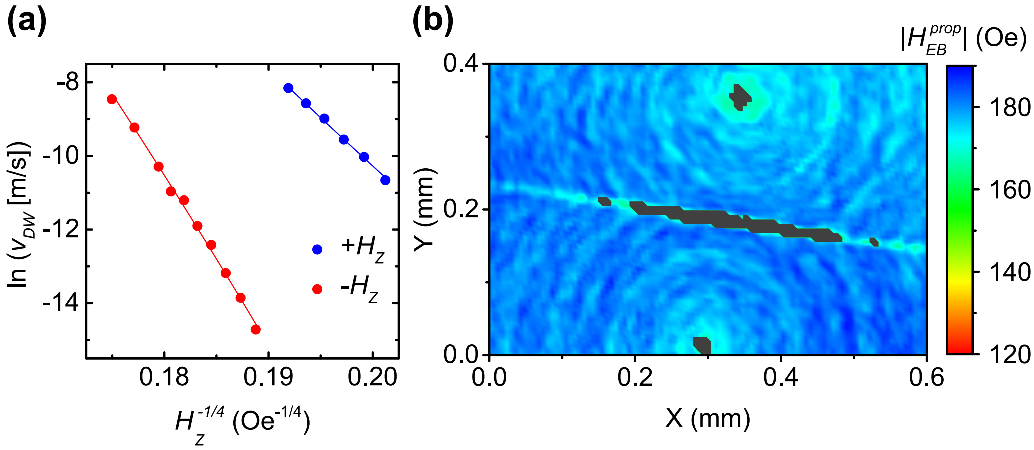

FIG. 3. (a) $\ln(v_{\mathrm{DW}})$ as a function of $H_z^{-(1/4)}$ measured near the bottom nucleation site in Fig. 1(c). The solid lines are fits to the data using Eq. (1) which give $H_{\mathrm{EB}}^{\mathrm{prop}} = -169.8 \pm 1.6$ Oe. (b) $H_{\mathrm{EB}}^{\mathrm{prop}}$ map around the region containing the two nucleation sites in Fig. 1(c) obtained from DW creep measurements. A reliable v_{DW} cannot be obtained within the initial two nucleated domains and where two DWs meet, shown as black in the figure.

we can conclude that there is not a single, well-defined H_{EB} for nucleation-dominated reversal.

To characterize H_{EB} away from nucleation sites, we measured the DW creep velocity for field-driven expansion of circular domains oriented parallel and antiparallel to H_{EB}. For this purpose, the system can be described as a 1D DW in a 2D medium [21,22] where the DW velocity v_{DW} in the creep regime follows the scaling law [21,23,24],

$$v_{\mathrm{DW}} = v_0 \exp\left(-\frac{E_b}{kT}\left(\frac{H_{\mathrm{crit}}}{|H_{\mathrm{eff}}|}\right)^{1/4}\right), \tag{1}$$

where H_{crit} is the critical depinning field, E_b is the disorder-induced barrier height, v_0 relates to attempt frequency, k is the Boltzmann constant, T is temperature, and H_{eff} is the effective field [25]. Here, H_{eff} consists of the applied H_z and the EB field, i.e., $H_{\mathrm{eff}} = H_z - H_{\mathrm{EB}}^{\mathrm{prop}}$, where by convention, $+H_z$ is (anti)parallel to (positive) negative $H_{\mathrm{EB}}^{\mathrm{prop}}$. The measurements were done for large (radius $> 10\,\mu$m) domains, minimizing effects of DW tension [22]. Figure 3(a) shows v_{DW} versus H_z for expanding (down) up domains oriented (anti)parallel to $H_{\mathrm{EB}}^{\mathrm{prop}}$. As expected, $H_{\mathrm{EB}}^{\mathrm{prop}}$ hinders (assists) the expansion of down (up) domains. Cofitting the curves in Fig. 3(a) to Eq. (1) assuming identical v_0 and $E_b(H_{\mathrm{crit}})^{1/4}/kT$ yields $H_{\mathrm{EB}}^{\mathrm{prop}} = -169.8 \pm 1.6$ Oe.

To estimate the local variation of $H_{\mathrm{EB}}^{\mathrm{prop}}$, we converted a map of differential DW displacements, acquired by imaging domain expansion using many short field pulses, to a map of local v_{DW} taken as the ratio of the differential displacement to the pulse width. Although in Fig. 3(a), both polarities of field were used to get the full set of creep data points needed to fit with Eq. (1), here we only used v_{DW} for expanding down domains (i.e., DWs driven by $-H_Z$). In this case, since the domains are always expanding into $+M_Z$ regions, measurements lasting minutes can be performed as thermally activated AFM grain reversal is not an issue, in contrast to the inverse case of expanding up domains (i.e., DWs driven by $+H_Z$). However, this lack of data for $+H_Z$ forces us to fix v_0 and $E_b(H_{\mathrm{crit}})^{1/4}$ to the values extracted from the fit to the data in Fig. 3(a). Figure 3(b) shows the resulting local $H_{\mathrm{EB}}^{\mathrm{prop}}$ map, which suggests that local variations of $H_{\mathrm{EB}}^{\mathrm{prop}}$ away from nucleation sites are far smaller than the variation of $H_{\mathrm{EB}}^{\mathrm{nuc}}$ amongst individual nucleation sites. Note that the variation in $H_{\mathrm{EB}}^{\mathrm{prop}}$ in Fig. 3(b) is an upper limit, since we assumed spatially uniform parameters v_0 and $E_b(H_{\mathrm{crit}})^{1/4}$, so that local variations in v_{DW} are cast entirely into local variations in $H_{\mathrm{EB}}^{\mathrm{prop}}$.

Since $H_{\mathrm{EB}}^{\mathrm{nuc}}$ and $H_{\mathrm{EB}}^{\mathrm{prop}}$ are generally different, H_{shift} is spatially inhomogeneous and depends on the distance d from the nearest nucleation site. As d tends to 0, H_{shift} tends toward $H_{\mathrm{EB}}^{\mathrm{nuc}}$, whereas one expects that H_{shift} should approach $H_{\mathrm{EB}}^{\mathrm{prop}}$ at large d. This is exactly what we find in Fig. 4(a), which shows H_{shift} as a function of d measured in the vicinity of a nucleation site in S2 and in S3. The general shape of the curves is similar despite different DW creep parameters and nucleation parameters for the two sites, indicating behavior that is not specific to a particular sample or nucleation site. Even when the DW creep parameters are the same, such as for three different nucleation sites in S2 [Fig. 4(b)], the rate of approach of H_{shift} to $H_{\mathrm{EB}}^{\mathrm{prop}}$ as d increases seems to depend on the nucleation parameters H_C^{nuc} and $H_{\mathrm{EB}}^{\mathrm{nuc}}$.

To understand this behavior better, we constructed a simple model that accounts for nucleation and propagation during the field-sweep process. The model considers a nucleation site at location $d = 0$ in a uniformly magnetized film with the system described using six variables—coercivity of the nucleation site H_C^{nuc}, EB of the nucleation site $H_{\mathrm{EB}}^{\mathrm{nuc}}$, sweep rate of the external field C (in Oe/s), a uniform propagation EB $H_{\mathrm{EB}}^{\mathrm{prop}}$ and uniform creep parameters v_0 and $E_b(H_{\mathrm{crit}})^{1/4}/kT$. Assuming deterministic nucleation that does not depend on the sweep rate, we simulate an external field sweep and calculate the field at which a domain wall reaches a distance d from the nucleation site. For example, for down-to-up reversal, nucleation occurs when the external field equals $H_C^{\mathrm{nuc}} + H_{\mathrm{EB}}^{\mathrm{nuc}}$. By convention, $H_{\mathrm{EB}}^{\mathrm{nuc}}$ is negative when it is parallel to $+H_z$. If time $t = t_1$ at the instance of nucleation and assuming the DWs are driven entirely in the creep regime, we can calculate the position of the DW at a time $t = t_2$ by integrating Eq. (1) with

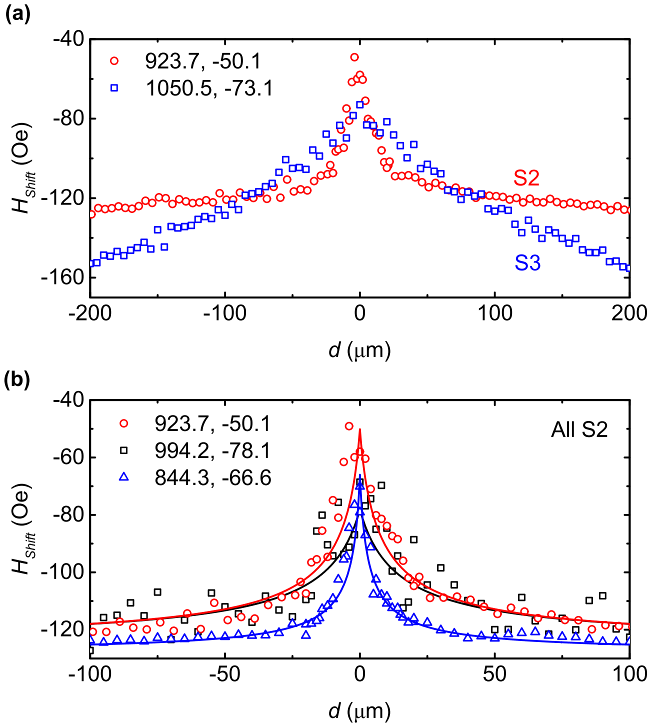

FIG. 4. (a) Experimentally measured $H_{\rm shift}$ for one exemplary nucleation site each in S2 and S3 as a function of distance from the site. The $H_{\rm EB}^{\rm prop}$ for S2 and S3 is around -120 and -180 Oe, respectively. (b) $H_{\rm shift}$ in S2 as a function of distance from three different nucleation sites. Solid lines are guides for the eye. The numbers in the legends refer to $H_C^{\rm nuc}$ and $H_{\rm EB}^{\rm nuc}$ in Oe, respectively.

respect to time,

$$d = \int_{t_1}^{t_2} v_{\rm DW}\, dt = \int_{t_1}^{t_2} v_0 \exp\left(-\frac{E_b}{kT}\left(\frac{H_{\rm crit}}{|H_z - H_{\rm EB}^{\rm prop}|}\right)^{1/4}\right) dt. \tag{2}$$

External field and time are related by the sweep rate via the relation $H_z = Ct$. Hence, by changing variables we can arrive at an expression that provides the field $H_{\rm switch,+}$ at which the DW reaches d, which is the switching field for that location,

$$d = \int_{(H_C^{\rm nuc}+H_{\rm EB}^{\rm nuc})}^{H_{\rm switch,+}} v_0 \exp\left(-\frac{E_b}{kT}\left(\frac{H_{\rm crit}}{|H_z - H_{\rm EB}^{\rm prop}|}\right)^{1/4}\right) 1/C\, dH_z, \tag{3}$$

where by definition, $H_C^{\rm nuc} + H_{\rm EB}^{\rm nuc} = Ct_1$ and $H_{\rm switch,+} = Ct_2$. This expression allows one to numerically calculate $H_{\rm switch,+}$ for each d, given a set of creep and nucleation parameters. The procedure is repeated for up-to-down reversal to yield the negative switching field $H_{\rm switch,-}$. From these two values, the local coercivity and hysteresis loop shift are defined as, $H_C = (H_{\rm switch,+} - H_{\rm switch,-})/2$ and $H_{\rm shift} = (H_{\rm switch,+} + H_{\rm switch,-})/2$, respectively.

Figure 5 shows calculated $H_{\rm shift}$ as a function of d for some combinations of $H_C^{\rm nuc}$ and $H_{\rm EB}^{\rm nuc}$, using $H_{EB}^{\rm prop} = -120$ Oe, $C = 14\,400$ Oe/s, $v_0 = 1.34 \times 10^{21}$ m/s, and $E_b(H_{\rm crit})^{1/4}/kT = 306\,{\rm Oe}^{1/4}$, which are close to the experimentally measured values for S2. The simulated curves show that the greater the difference between $H_{\rm EB}^{\rm nuc}$ and $H_{\rm EB}^{\rm prop}$, the slower $H_{\rm shift}$ approaches $H_{\rm EB}^{\rm prop}$ [compare the different curves within each plot of Figs. 5(a), 5(b), and 5(c)]. Note that for two $H_{\rm EB}^{\rm nuc}$ that are equally higher or lower than $H_{\rm EB}^{\rm prop}$, the curves are mirror images of one another. Moreover, we see that the rate of approach becomes significantly slower as $H_C^{\rm nuc}$ is increased [compare between (a), (b), and (c) in Fig. 5]. All of this agrees with the experimentally measured data in Fig. 4(b), and this behavior is explained by considering the effective field $H_{\rm eff,\,DW}$ that drives DW propagation immediately after nucleation,

$$H_{\rm eff,\,DW} = H_{\rm switch} - H_{\rm EB}^{\rm prop} = \left(\pm H_C^{\rm nuc} + H_{\rm EB}^{\rm nuc}\right) - H_{\rm EB}^{\rm prop}. \tag{4}$$

Here, $H_{\rm switch} = \pm H_C^{\rm nuc} + H_{\rm EB}^{\rm nuc}$ is the nucleation field for down-to-up (+) or up-to-down (−) magnetization reversal. From Eq. (4), the higher is $H_C^{\rm nuc}$, the higher is $H_{\rm eff,\,DW}$, resulting in faster $v_{\rm DW}$ and less influence of $H_{\rm EB}^{\rm prop}$. In the limit of infinite $H_C^{\rm nuc}$, the DW would reach the measurement spot instantaneously and $H_{\rm EB}^{\rm prop}$ would have no effect. Figure 5(d) shows the normalized difference between $H_{\rm shift}$ and $H_{\rm EB}^{\rm prop}$, namely, $H_{\rm rel} = (H_{\rm shift} - H_{\rm EB}^{\rm prop})/H_{\rm EB}^{\rm prop}$, as a function of normalized distance. The distance is conveniently normalized based on the approximate velocity of a DW immediately upon nucleation and the nucleation field. Thus $\tilde{d}$, a dimensionless parameter, is defined as

$$\tilde{d} = d\frac{C}{v_0 \exp\left(-\frac{E_b}{kT}\left(\frac{H_{\rm crit}}{H_C^{\rm nuc}}\right)^{1/4}\right)H_C^{\rm nuc}}, \tag{5}$$

where C is the sweep rate of the HL measurement. Plotted in this way, $H_{\rm shift}$ does not depend on any of the parameters that appear in Eq. (5), so that most of the curves in Figs. 5(a), 5(b), and 5(c) overlap, as shown in Fig. 5(d).

We can also quantify the influence of a nucleation site by defining a critical influence distance d_C as the d at which $H_{\rm shift}$ is within 5% of $H_{\rm EB}^{\rm prop}$ (i.e., $|H_{\rm rel}| = 5\%$). d_C depends very sensitively on the creep parameters, as shown in Fig. 5(e), which plots d_C as a function of $H_{\rm EB}^{\rm nuc}/H_{\rm EB}^{\rm prop}$ for different $E_b(H_{\rm crit})^{1/4}/kT$ values. Thus, depending on the system, the influence of nucleation sites on $H_{\rm shift}$ can vary from nanometers to millimeters, and given a high enough nucleation density, even in the case of a large-area macroscopic measurement like VSM, $H_{\rm shift}$ can be significantly different from $H_{\rm EB}^{\rm prop}$, if the average $H_{\rm EB}^{\rm nuc}/H_{\rm EB}^{\rm prop}$ is sufficiently far away from 1. A more general way to visualize the influence of nucleation is to plot the normalized critical influence distance $\tilde{d}_C$ [Fig. 5(f)], which depends only on the ratio $H_{\rm EB}^{\rm nuc}/H_{\rm EB}^{\rm prop}$.

Another surprising feature of unequal $H_{\rm EB}^{\rm nuc}$ and $H_{\rm EB}^{\rm prop}$ is that HLs can become asymmetric. Figure 6(a) depicts a HL belonging to the center of the site shown in red points in Fig. 5(b), where the up-to-down magnetization reversal occurs over a larger field range than the down-to-up case. To simulate such HLs, we considered circular regions of a certain size (10-μm diameter in this case) with a single nucleation site at the center, resembling a MOKE laser centered on a nucleation site. Then, from the switching fields ($H_{\rm switch,+}$ and $H_{\rm switch,-}$) calculated as a function of d as described previously, one can determine the size of the reverse domain at any given field, and hence the fraction of area switched, x, as a

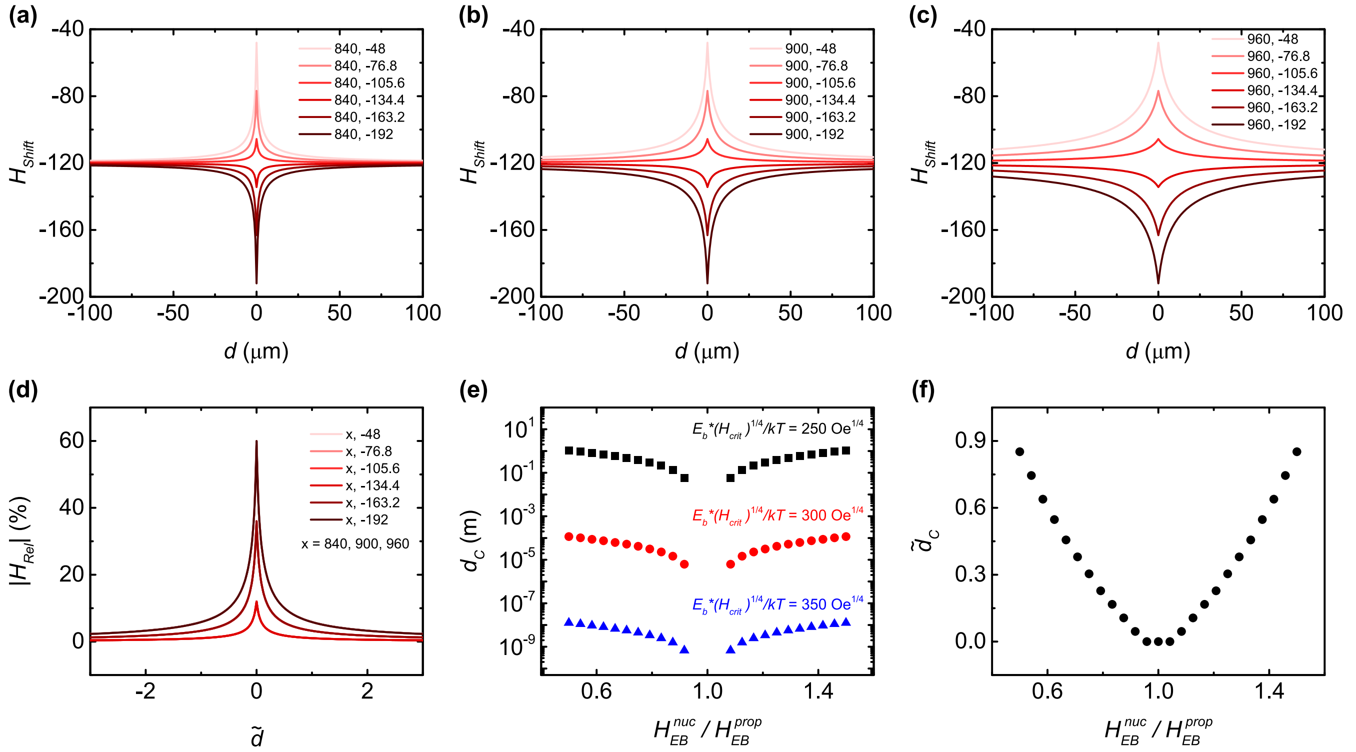

FIG. 5. Calculated H_{shift} as a function of d for H_C^{nuc} equal to (a) 840 Oe, (b) 900 Oe, and (c) 960 Oe are shown for a series of $H_{\text{EB}}^{\text{nuc}}$ values. The two numbers in the legend refer to H_C^{nuc} and $H_{\text{EB}}^{\text{nuc}}$ in Oe, respectively. (d) Same data as (a)–(c) plotted with normalized variables (see text). The curves for different H_C^{nuc} but same $H_{\text{EB}}^{\text{nuc}}$, and curves with exactly the same $|H_{\text{shift}} - H_{\text{EB}}^{\text{prop}}|$ overlap. (e) Critical influence distance d_C as a function of $H_{\text{EB}}^{\text{nuc}}/ H_{\text{EB}}^{\text{prop}}$, shown for three different $E_b(H_{\text{crit}})^{1/4}/kT$ values. H_C^{nuc} was taken as 900 Oe and other parameters were the same as (a)–(c). The curves approach and reach zero at $H_{\text{EB}}^{\text{nuc}}/ H_{\text{EB}}^{\text{prop}} = 1$. (f) Same plot as (e) using normalized distance.

function of applied field. The magnetization, then, is proportional to the expression $(+1)x + (-1)(1-x)$. Note that our model does not consider the Gaussian profile of a typical MOKE laser beam, which would smear out the transitions in the HL. Calculated in this way, the simulations [Figs. 6(b) and 6(c)] agree with experiments, and also predict a significant influence of the experimental conditions such as sweep rate and temperature on the degree of asymmetry. What is notable is that in this regime, the up-to-down transition varies much more strongly than the down-to-up one when the parameters are changed. The origin of this asymmetry can be tied to the difference in the average v_{DW} during the two reversals. For the case $|H_{\text{EB}}^{\text{nuc}}| < |H_{\text{EB}}^{\text{prop}}|$ shown in Fig. 6, it can be seen from Eq. (4) that $H_{\text{eff, DW}}$ is higher for down-to-up reversal than

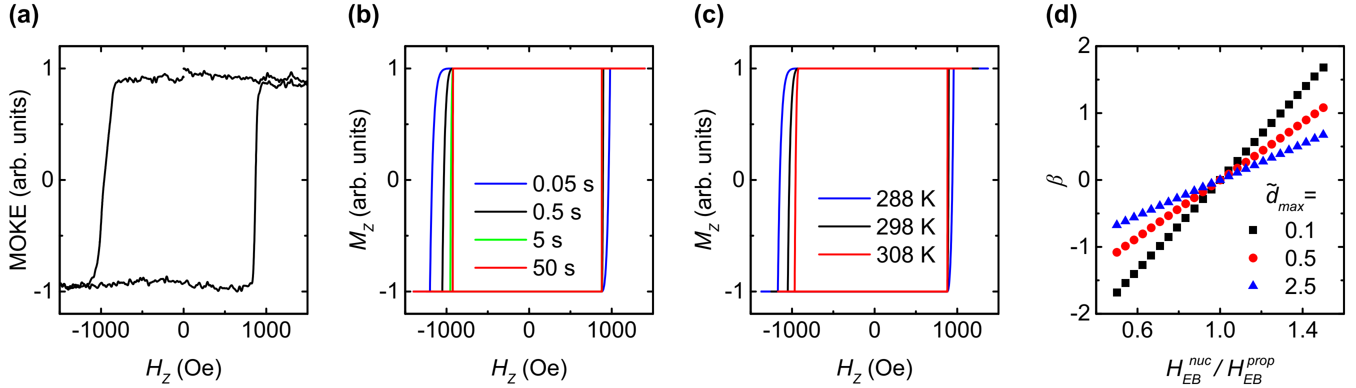

FIG. 6. (a) A typical HL of the nucleation site corresponding to the red data points in Fig. 4(b). (b), (c) Simulated HLs of a nucleation site with $H_C^{\text{nuc}} = 900$ Oe and $H_{\text{EB}}^{\text{nuc}} = -20$ Oe, showing the evolution of switching asymmetry as a function of experimental conditions such as sweep rate (b) and temperature (c). The legend in (b) refers to $t_{\text{sweep}} = 7200/C$. Other parameters for calculations were the same as those used for Fig. 5. In (c), we do not consider the temperature dependence of any of the parameters—-only the explicit T dependence in Eq. (3) is accounted for. (d) Asymmetry parameter β (see text) as a function of $H_{\text{EB}}^{\text{nuc}}/ H_{\text{EB}}^{\text{prop}}$. $\tilde{d}_{\max}$ refers to the radius of the circular region considered for performing the calculations.

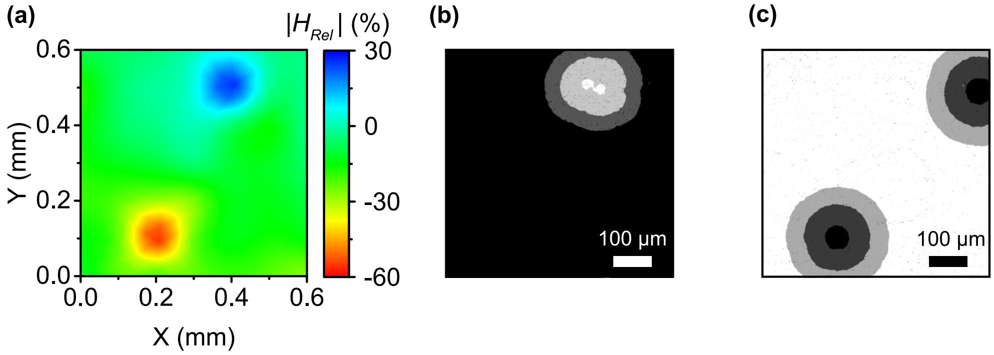

FIG. 7. (a) Color map of H_{rel} from point-by-point MOKE measurements of a particular area of S1. (b), (c) Domain nucleation patterns for down-to-up (b) and up-to-down reversal (c). Like Fig. 1(d), white is up magnetization and black (gray) is down magnetization. After an initial nucleation pulse, (b) shows the extent of the reversed domain after $n = 0$, 1, and 2 (686-Oe, 700-ms) pulses, and (c) shows the extent of the reversed domains after $n = 1$, 3, and 5 (-990-Oe, 500-ms) pulses were applied.

up-to-down, resulting in faster v_{DW} and a sharper transition in the former case compared to the latter. Hence, the degree of asymmetry depends on all the parameters that appear in Eq. (3) but it is much more convenient to normalize the diameter of the HL acquisition area by Eq. (5). As depicted in Fig. 6(d), the degree of asymmetry then depends only on $H_{\mathrm{EB}}^{\mathrm{nuc}}/H_{\mathrm{EB}}^{\mathrm{prop}}$ and the normalized diameter, characterized by $\tilde{d}_{\max}$. Here, the asymmetry is quantified by the factor $\beta = \log(\frac{\Delta H_{\mathrm{down-to-up}}}{\Delta H_{\mathrm{up-to-down}}})$, where ΔH denotes the width (in units of field) of the respective transition.

Finally, more complex interactions between nucleation sites may arise due to proximity of sites with large differences in $H_{\mathrm{EB}}^{\mathrm{nuc}}$. Figure 7(a) depicts a case in which two nucleation sites with $H_{\mathrm{EB}}^{\mathrm{nuc}}$ significantly higher and lower than $H_{\mathrm{EB}}^{\mathrm{prop}}$ are near one another. Due to the dissimilar $H_{\mathrm{EB}}^{\mathrm{nuc}}$, their reversal fields are staggered such that the high-EB site suppresses the down-to-up magnetization reversal of the other site [Fig. 7(b)] and vice versa [Fig. 7(c)]. In between these two sites, the origin of the propagating DW is different for either side of the HL, leading to characteristics that would now be an entanglement of two sites in addition to the DW propagation parameters. The full consequence of such cases remains to be explored.

IV. CONCLUSION

We have demonstrated that nucleation and propagation EB can be disentangled by combining traditional MOKE measurements with DW dynamics-based measurements. Our experiments reveal that nucleation sites can have EB that is significantly different than the propagation EB, and that the variance in $H_{\mathrm{EB}}^{\mathrm{nuc}}$ is generally larger than that of $H_{\mathrm{EB}}^{\mathrm{prop}}$. Experiments and simulations both show that the spatial influence of nucleation sites generally increases with increasing difference between $H_{\mathrm{EB}}^{\mathrm{nuc}}$ and $H_{\mathrm{EB}}^{\mathrm{prop}}$, and that an asymmetry in the magnetization reversal characteristics can arise because of this difference. Our formalism for the analysis of these features can be applied beyond our specific system, and we further show that more complicated behavior may occur in situations with multiple nearby nucleation sites. Our work sheds light on phenomena in EB systems that have been studied for a long time, and the findings can have implications for characterizing and analyzing any system where two or more materials are magnetically coupled.

The data that support the findings of this study are available from the corresponding author upon reasonable request.

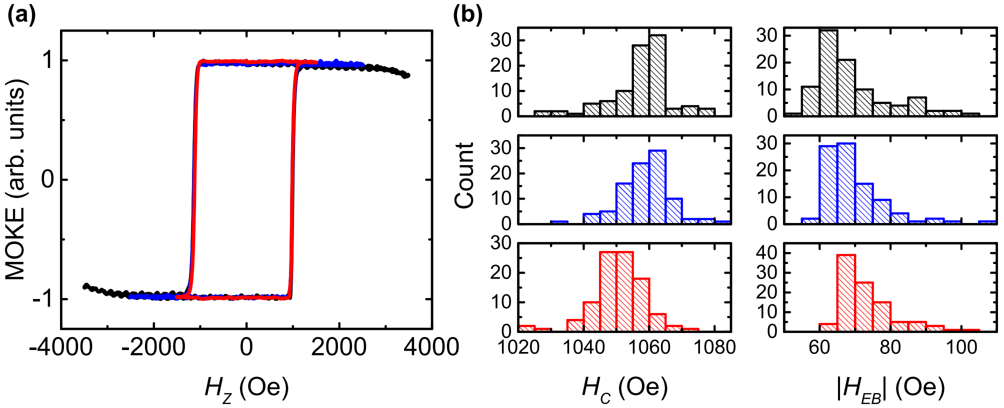

FIG. 8. (a) HL obtained using a maximum field of approximately 1500 (red), 2500 (blue), and 3500 (black) Oe, with a constant sweep rate. (b) Distribution of H_C^{nuc} and $H_{\mathrm{EB}}^{\mathrm{nuc}}$ obtained using different maximum fields (increases from bottom to top).

ACKNOWLEDGMENTS

This work was supported by Spintronic Materials for Advanced Information Technologies (SMART) (Grant No. 2018-NE-2861), one of seven centers of nCORE, a Semiconductor Research Corporation program, sponsored by the National Institute of Standards and Technology (NIST) and the Samsung Global Research Outreach (GRO) program.

APPENDIX: HYSTERESIS LOOPS USING HIGHER FIELDS

HLs for the measurements shown in Figs. 1 and 2 of the main text were obtained using the highest practical field for the experimental setup used. An important factor for the limited fields was the use of a temperature controller for keeping the temperature stable. Figure 8(a) shows HLs obtained after removing the temperature-controller stage, which allows higher fields to be reached at the sample (sweep rate kept constant). There is no discernible effect on the switching fields when the maximum field is increased beyond the saturating field and the distribution of H_C^{nuc} and $H_{\text{EB}}^{\text{nuc}}$, shown in Fig. 8(b), remains the same within experimental error. These data were obtained from sample S3, which has characteristics like S1 (used for Fig. 1 to Fig. 3). Sample S1 was inadvertently altered after the initial experiments, rendering it unsuitable for follow-up measurements.

[1] W. H. Meiklejohn and C. P. Bean, New magnetic anisotropy, Phys. Rev. **105**, 904 (1957).

[2] A. P. Malozemoff, Random-field model of exchange anisotropy at rough ferromagnetic-antiferromagnetic interfaces, Phys. Rev. B **35**, 3679 (1987).

[3] R. L. Stamps, Mechanisms for exchange bias, J. Phys. D: Appl. Phys. **33**, R247 (2000).

[4] J. Nogués and I. K. Schuller, Exchange bias, J. Magn. Magn. Mater. **192**, 203 (1999).

[5] C. Chappert, A. Fert, and F. N. Van Dau, The emergence of spin electronics in data storage, Nat. Mater. **6**, 813 (2007).

[6] S. Fukami, C. Zhang, S. DuttaGupta, A. Kurenkov, and H. Ohno, Magnetization switching by spin–orbit torque in an antiferromagnet–ferromagnet bilayer system, Nat. Mater. **15**, 535 (2016).

[7] I. Polenciuc, A. J. Vick, D. A. Allwood, T. J. Hayward, G. Vallejo-Fernandez, K. O'Grady, and A. Hirohata, Domain wall pinning for racetrack memory using exchange bias, Appl. Phys. Lett. **105**, 162406 (2014).

[8] M. Mansuripur, Magnetization reversal, coercivity, and the process of thermomagnetic recording in thin films of amorphous rare earth–transition metal alloys, J. Appl. Phys. **61**, 1580 (1987).

[9] H. J. Williams and R. C. Sherwood, Magnetic domain patterns on thin films, J. Appl. Phys. **28**, 548 (2004).

[10] M. S. Pierce *et al.*, Influence of structural disorder on magnetic domain formation in perpendicular anisotropy thin films, Phys. Rev. B **87**, 184428 (2013).

[11] T. Shima, K. Takanashi, Y. K. Takahashi, K. Hono, G. Q. Li, and S. Ishio, High coercivity and magnetic domain observation in epitaxially grown particulate FePt thin films, J. Magn. Magn. Mater. **266**, 171 (2003).

[12] J. Camarero, J. Sort, A. Hoffmann, J. M. García-Martín, B. Dieny, R. Miranda, and J. Nogués, Origin of the asymmetric magnetization reversal behavior in exchange-biased systems: Competing anisotropies, Phys. Rev. Lett. **95**, 057204 (2005).

[13] M. Gierlings, M. J. Prandolini, H. Fritzsche, M. Gruyters, and D. Riegel, Change and asymmetry of magnetization reversal for a Co/CoO exchange-bias system, Phys. Rev. B **65**, 092407 (2002).

[14] S. van Dijken, M. Czapkiewicz, M. Zoladz, and T. Stobiecki, Asymmetric magnetization reversal in exchange-biased Co/Pt multilayers, Phys. Status Solidi **243**, 169 (2006).

[15] M. R. Fitzsimmons, P. Yashar, C. Leighton, I. K. Schuller, J. Nogués, C. F. Majkrzak, and J. A. Dura, Asymmetric magnetization reversal in exchange-biased hysteresis loops, Phys. Rev. Lett. **84**, 3986 (2000).

[16] M. U. Hasan, A. E. Kossak, and G. S. D. Beach, Large exchange bias enhancement and control of ferromagnetic energy landscape by solid-state hydrogen gating, Nat. Commun. **14**, 8510 (2023).

[17] U. Bauer, L. Yao, A. J. Tan, P. Agrawal, S. Emori, H. L. Tuller, S. Van Dijken, and G. S. D. Beach, Magneto-ionic control of interfacial magnetism, Nat. Mater. **14**, 174 (2015).

[18] A. Ehresmann, C. Schmidt, T. Weis, and D. Engel, Thermal exchange bias field drift in field cooled $\text{Mn}_{83}\text{Ir}_{17}/\text{Co}_{70}\text{Fe}_{30}$ thin films after 10 KeV He Ion bombardment, J. Appl. Phys. **109**, 023910 (2011).

[19] A. Paetzold and K. Röll, Thermally activated self-alignment of exchange coupling in NiO/NiFe bilayers, J. Appl. Phys. **91**, 7748 (2002).

[20] P. A. A. van der Heijden, T. F. M. M. Maas, W. J. M. de Jonge, J. C. S. Kools, F. Roozeboom, and P. J. van der Zaag, Thermally assisted reversal of exchange biasing in NiO and FeMn based systems, Appl. Phys. Lett. **72**, 492 (1998).

[21] S. Lemerle, J. Ferré, C. Chappert, V. Mathet, T. Giamarchi, and P. Le Doussal, Domain wall creep in an Ising ultrathin magnetic film, Phys. Rev. Lett. **80**, 849 (1998).

[22] K. W. Moon, J. C. Lee, S. G. Je, K. S. Lee, K. H. Shin, and S. B. Choe, Long-range domain wall tension in Pt/Co/Pt films with perpendicular magnetic anisotropy, Appl. Phys. Express **4**, 043004 (2011).

[23] P. J. Metaxas, J. P. Jamet, A. Mougin, M. Cormier, J. Ferré, V. Baltz, B. Rodmacq, B. Dieny, and R. L. Stamps, Creep and flow regimes of magnetic domain-wall motion in ultrathin Pt/Co/Pt films with perpendicular anisotropy, Phys. Rev. Lett. **99**, 217208 (2007).

[24] F. Cayssol, D. Ravelosona, C. Chappert, J. Ferré, and J. P. Jamet, Domain wall creep in magnetic wires, Phys. Rev. Lett. **92**, 107202 (2004).

[25] P. J. Metaxas, J. P. Jamet, J. Ferré, B. Rodmacq, B. Dieny, and R. L. Stamps, Magnetic domain wall creep in the presence of an effective interlayer coupling field, J. Magn. Magn. Mater. **320**, 2571 (2008).